The Astrophysical Journal Letters, 928:L15 (7pp), 2022 April 1 https://doi.org/10.3847/2041-8213/ac5fb0

The Turbulent Properties of the Sub-Alfvénic Solar Wind Measured by the Parker Solar Probe

L.-L. Zhao[1,2], G. P. Zank[1,2], D. Telloni[3], M. Stevens[4], J. C. Kasper[5], and S. D. Bale[6]
[1] Center for Space Plasma and Aeronomic Research (CSPAR), The University of Alabama in Huntsville, Huntsville, AL 35805, USA; lz0009@uah.edu
[2] Department of Space Science, The University of Alabama in Huntsville, Huntsville, AL 35805, USA
[3] INAF—Astrophysical Observatory of Torino, Via Osservatorio 20, I-10025 Pino Torinese, Italy
[4] Smithsonian Astrophysical Observatory, Cambridge, MA 02138 USA
[5] BWX Technologies, Inc., Washington DC 20002, USA and Department of Climate and Space Sciences and Engineering, University of Michigan, Ann Arbor, MI 48109, USA
[6] Physics Department, University of California, Berkeley, CA 94720-7300, USA
Received 2022 January 14; revised 2022 March 10; accepted 2022 March 20; published 2022 March 31

Abstract

For the first time, Parker Solar Probe (PSP) observed the sub-Alfvénic solar wind where the solar wind bulk speed drops below the local Alfvén speed for an extended period of time. Here, we report on the turbulent properties of the sub-Alfvénic region. We analyze the turbulence correlation length and the energy transfer and compare the results with nearby super-Alfvénic regions. As the Alfvén speed is larger or comparable to the solar wind speed in the intervals studied, we use a modified Taylor's hypothesis to account for wave propagation. We find that the wave propagation speed affects the analysis of the correlation lengths of the forward and backward propagating $z^{\pm}$ modes. In the sub-Alfvénic region, the correlation length of the z^{-} mode is shorter than that of the outward propagating z^{+} mode, although the correlation time of the z^{-} mode is about 10 times larger than that of the z^{+} mode. For the energy transfer, we use both incompressible and compressible formulations to calculate the energy flux based on third-order structure functions. The incompressible energy cascade rates for the forward and backward propagating modes are computed separately using the modified Taylor's hypothesis. The averaged compressible cascade rate is higher in the sub-Alfvénic interval than the nearby downstream super-Alfvénic region, which may be due to the lower fluctuation amplitude in the latter super-Alfvénic interval. Longer incursions of the PSP in the sub-Alfvénic winds in the future will give us better statistics.

Unified Astronomy Thesaurus concepts: Solar wind (1534); Interplanetary turbulence (830)

1. Introduction

The Parker Solar Probe (PSP) entered the sub-Alfvénic solar wind for the first time on 2021 April 28 (Kasper et al. 2021). The region is characterized by a long-lasting period when the solar wind speed is lower than the local Alfvén speed. The various turbulence spectra in the sub-Alfvénic and the nearby super-Alfvénic solar wind have been analyzed extensively by Zank et al. (2022). In this letter, we analyze the energy cascade and turbulent correlation length scale in both the sub- and neighboring super-Alfvénic solar wind.

In incompressible neutral fluid turbulence, the energy cascade rate ε is usually regarded as a constant in the inertial range and the fluctuation power spectrum follows a $k^{-5/3}$ power law (Kolmogorov 1941), where k is the wavenumber. The energy cascade rate ε represents the energy dissipation per unit mass. Furthermore, Kolmogorov (1941) suggested the third-order law for which the third-order structure function of the longitudinal velocity is proportional to the energy cascade rate with a factor of $-4/5\ l$ (l being the increment in distance), known as the Kolmogorov's four-fifth's law (Frisch 1995). For incompressible MHD turbulence, the four-fifth's law was extended by Politano & Pouquet (1998), finding a similar relation for the third-order mixed structure functions for the Elsässer variables (Elsasser 1950), i.e., in terms of the plasma velocity, magnetic field, and constant density. The relation has been used in recent years to calculate the energy cascade rate in solar wind data (e.g., Sorriso-Valvo et al. 2018; Bandyopadhyay et al. 2020). Based on a single-point closure related to von Kármán law, Adhikari et al. (2021) derived the cascade rate for the various fluctuating energies and found good agreement with PSP observations (Zhao et al. 2021). We note that Bandyopadhyay et al. (2020) computed the energy cascade rate from both the von Kármán law and third-order law using PSP first-orbit observations and found a fairly good consistency between these two different estimates. More recently, compressible versions of the energy cascade rate have also been derived (e.g., Banerjee & Kritsuk 2018; Andrés et al. 2019). In particular, Andrés et al. (2021) compare the energy cascade rate calculated with both incompressible and compressible formulae using solar wind data. While the two methods give results that generally agree with each other, the discrepancy between the two is larger when the compressibility is larger. Here, we use the formalism in Andrés et al. (2021) and apply the method to the PSP data in the sub-Alfvénic region.

A complicating issue for the analysis of sub-Alfvénic intervals is that the standard Taylor's hypothesis cannot be used because the bulk solar wind flow speed is smaller than the local Alfvén speed. The frequency (or time lag) cannot be mapped therefore to wavenumber (or length increment) simply by multiplying the solar wind bulk speed. There are suggestions for how to modify Taylor's hypothesis in such situations (e.g., Klein et al. 2015; Bourouaine & Perez 2018; Perez et al. 2021). For the incompressible model, we consider

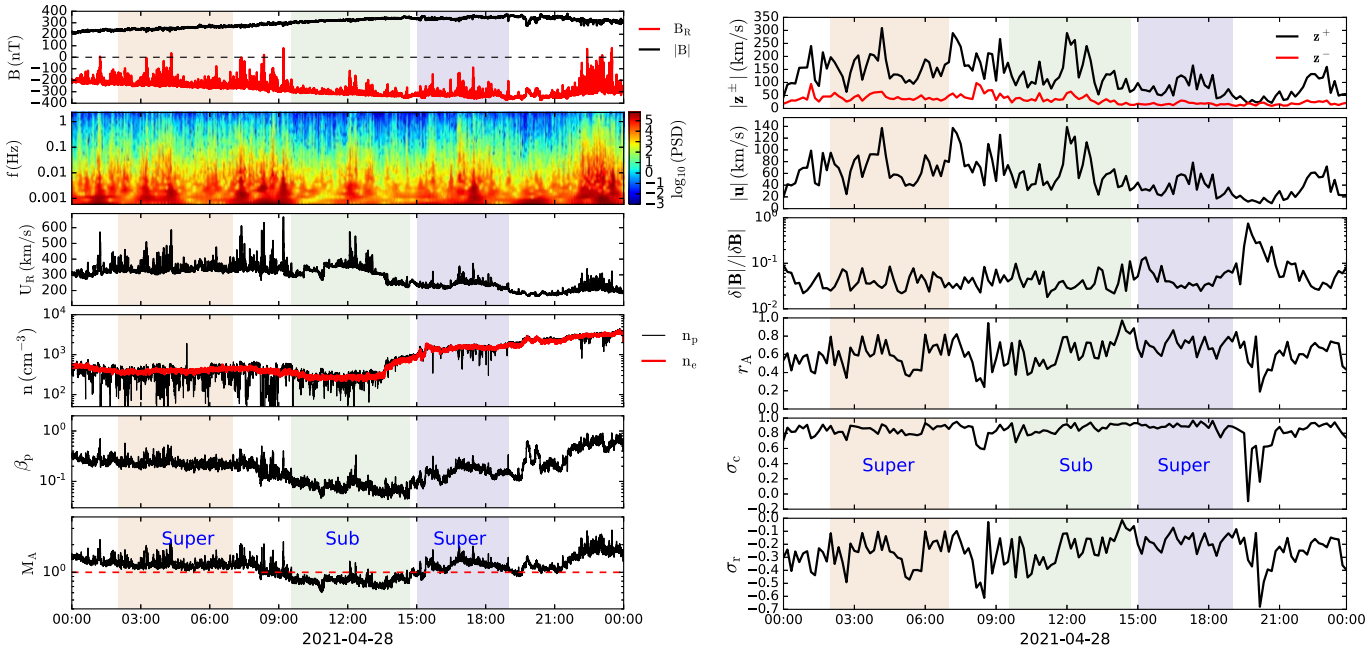

Figure 1. An overview of the first sub-Alfvénic flow observed by the PSP during its 8th orbit. The sub-Alfvénic interval is indicated by the green shaded area. Two nearby super-Alfvénic intervals are indicated by pink and purple shaded areas, respectively. Left panels from top to bottom show the magnetic field radial component B_R and magnitude $|B|$, power spectral density (PSD) of the B_R component, proton radial velocity U_R, proton density n_p from SPAN-I (black) and electron density n_e from QTN (red), proton plasma beta β_p, and radial Alfvén Mach number M_A. Right panels from top to bottom show the amplitude of Elsässer variables $|\boldsymbol{z}^{\pm}|$, velocity fluctuation amplitude $|\boldsymbol{u}|$, magnetic compressibility $\delta|\boldsymbol{B}|/|\delta\boldsymbol{B}|$, Alfvén ratio $r_{\rm A}$, normalized cross helicity σ_c, and normalized residual energy σ_r.

the forward and backward Elsässer variables separately (e.g., Adhikari et al. 2020; Zank et al. 2020), so that their different propagation speeds can be taken into account (Zank et al. 2022). The idea of taking the propagation speed into account to differentiate inward and outward propagating Elsässer fluctuations is similar to that introduced by Goldstein et al. (1986). We show that this simple modified Taylor's hypothesis has a significant effect on how to interpret the results.

In addition, we analyze the correlation length scale using the modified Taylor's hypothesis in Zank et al. (2022) for the forward and backward propagating modes, respectively. The forward and backward correlation times are taken as the time lag at which the autocorrelation function becomes $1/e$ of its maximum value (Bruno & Carbone 2013). Previous studies have found a large difference in the correlation time between the forward and backward modes using PSP measurements (e.g., Chen et al. 2020). We show that this large difference is mostly due to the wave propagation speed.

2. Data Overview

During Encounter 8, PSP observed three sub-Alfvénic intervals (Kasper et al. 2021). In this letter, we focus on the first sub-Alfvénic interval, which was crossed at a radial distance of approximately 0.09 au on 2021 April 28. The solar wind velocity in this interval continues to be lower than the local Alfvén speed for about 5 hr and is far from the large-scale heliospheric current sheet (HCS), and it is considered to be the most robust sub-Alfvénic flow of the three (Kasper et al. 2021).

Figure 1 shows an overview of the magnetic field, solar wind plasma, and turbulence variables observed in this sub-Alfvénic interval. The magnetic field data are measured by the PSP/FIELDS Fluxgate Magnetometer instrument (Bale et al. 2016). The solar wind ion (proton) velocity, density, and temperature are obtained from the PSP Solar Wind Electrons Alphas and Protons and Solar Probe ANalyzer for Ions (SPAN-I) instruments (Kasper et al. 2016). The electron density data are obtained from the plasma quasi-thermal noise (QTN) spectrum measured by FIELDS Radio Frequency Spectrometer and Low Frequency Receiver instruments (Moncuquet et al. 2020). Here, we have downsampled magnetic field measurements at the same ∼3.5 s resolution as plasma data. As shown in the left panels, the magnetic field during this one-day period is in the sunward direction. In the sub-Alfvénic region, the time profile of the B_R component shows far fewer "switchback" structures compared to the nearby super-Alfvénic flow (Kasper et al. 2021). A recent study by Bandyopadhyay et al. (2022) quantifies the magnetic field deflection parameter z and suggests that no samples with strong magnetic deflection are found in the sub-Alfvénic region. Other statistical properties, such as the turbulence amplitude, variance anisotropy, and intermittency, have also been reported by combining the four observed sub-Alfvénic intervals into a single data set (Bandyopadhyay et al. 2022). From the power spectral density (PSD) of the B_R component, it is clear that its fluctuating power in the sub-Alfvénic region is lower than the surrounding super-Alfvénic plasma. The proton radial velocity stays below 400 km s^{-1}. The proton density is roughly consistent with the electron density, except for some dropouts (e.g., 08:00–09:00), which is probably due to the proton distribution being out of the field of view of SPAN-I. As the electron density derived from the QTN spectrum is more reliable than the SPAN-I ion density, we use it as a proxy of the plasma density in the following analysis. The proton plasma beta β_p (ratio between the proton thermal pressure and magnetic pressure) and the radial Alfvén Mach number $M_A = U_R/V_A$ are much lower in the sub-Alfvénic interval with the averaged $\beta_p \simeq 0.08$ and $M_A \simeq 0.8$.

In the right panels of Figure 1, we show the time profile of various turbulence quantities during the crossing of the first sub-Alfvénic interval. The forward and backward fluctuating Elsässer variables are constructed as $\boldsymbol{z}^{\pm} = \boldsymbol{u} \pm \boldsymbol{b}$ with $\boldsymbol{b} = \delta\boldsymbol{B}/\sqrt{4\pi\rho_0}$, where $\boldsymbol{u} = \boldsymbol{U} - \boldsymbol{U}_0$ is the fluctuating velocity field, $\delta\boldsymbol{B} = \boldsymbol{B} - \boldsymbol{B}_0$ is the fluctuating magnetic field, ρ_0 is the time averaged proton mass density, $\boldsymbol{U}$ and $\boldsymbol{B}$ are the solar wind speed and magnetic field measurements in the inertial RTN coordinate system, $\boldsymbol{U}_0$ and $\boldsymbol{B}_0$ are the mean velocity and mean magnetic field, respectively. The normalized cross helicity σ_c, normalized residual energy σ_r, and the Alfvén ratio $r_{\rm A}$ are then defined as (Zank et al. 2012):

$$\sigma_c = \frac{2\langle \boldsymbol{u}\cdot\boldsymbol{b}\rangle}{\langle \boldsymbol{u}^2\rangle + \langle \boldsymbol{b}^2\rangle},$$

$$\sigma_r = \frac{\langle \boldsymbol{u}^2\rangle - \langle \boldsymbol{b}^2\rangle}{\langle \boldsymbol{u}^2\rangle + \langle \boldsymbol{b}^2\rangle},$$

$$r_{\rm A} = \langle \boldsymbol{u}^2\rangle / \langle \boldsymbol{b}^2\rangle.$$

Each fluctuating quantity is calculated at nonoverlapping 10 minute intervals to characterize the inertial range turbulence. The background mean fields (magnetic field and velocity) used to calculate fluctuations are the average of their time series over each 10 minute interval. As shown in the figure, the dominant fluctuations are the outward propagating z^+ fluctuations during this one-day period (Zank et al. 2022). The amplitude of z^+ modes ranges from ~20 to 309 km s^{-1}, and the amplitude of z^- fluctuations ranges from ~10 to 98 km s^{-1}. The averaged amplitudes of z^+ and z^- in the sub-Alfvén interval are about 132 km s^{-1} and 34 km s^{-1}, respectively, which are similar to the prior super-Alfvénic interval and a little higher than the latter super-Alfvénic interval. The velocity fluctuation amplitude $|\boldsymbol{u}|$ shows similar changes as the forward propagating z^+ mode and is about 60 km s^{-1} in the sub-Alfvén interval. The magnetic compressibility is calculated by the square root of the ratio between magnetic field magnitude variance and the total magnetic fluctuations variance, i.e., $\delta|\mathbf{B}|/|\delta\mathbf{B}|$. The compressibility does not show significant differences in these three intervals, with the average value well below 0.1, indicating the incompressible nature of the solar wind turbulence. The Alfvén ratio $r_{\rm A}$ and the normalized cross helicity σ_c are close to 1 during this one-day period except that $r_{\rm A}$ and σ_c decrease significantly near 20:00 with $|z^+| \simeq |z^-|$, which may be due to the existence of small-scale magnetic flux rope structures (Zhao et al. 2020, 2021). The average values of σ_c and r_A do not show significant changes in the studied sub-Alfvénic flow and the neighboring super-Alfvénic flows. This is consistent with the spectrogram of σ_c at small scales (≃10 minutes) shown in Zank et al. (2022). To avoid the effects of the possible magnetic flux rope structures near 20:00, we restrict the latter super-Alfvénic interval to be 1 hr shorter than the sub- and prior super-Alfvénic intervals. The normalized residual energy σ_r in the whole-day measurements is negative and close to 0 during the three selected intervals, indicating the slight dominance of the magnetic fluctuations in both super- and sub-Alfvénic regions. As the parameters $\sigma_c \simeq 1$ and $\sigma_r \simeq 0$ with a sunward background magnetic field, this suggests generally outward propagating Alfvénic fluctuations during these three intervals.

3. Correlation Length

Consider now the correlation length scale of various turbulent fluctuations during the first crossing of the Alfvén surface. Figure 2 plots the normalized autocorrelation function for the fluctuating Elsässer variables $\boldsymbol{z}^{\pm}$, fluctuating velocity $\boldsymbol{u}$, and fluctuating magnetic field $\delta\boldsymbol{B}$. The correlation function is calculated by

$$C(\tau) = \frac{1}{N}\sum_t \boldsymbol{z}^{\pm}(t)\cdot\boldsymbol{z}^{\pm}(t+\tau)$$

for the Elsässer variables and similarly for the velocity and magnetic field, where N is the number of points in the summation and τ is the time lag. The correlation function is then normalized by $C(\tau=0)$, i.e., $R(\tau) = C(\tau)/C(\tau=0)$. The horizontal dashed line in each panel denotes $1/e$ times the maximum value, where the correlation time τ_c is determined, i.e., $C(\tau_c) = C(\tau=0)/e$. For the sake of completeness, we also show the power spectral density (PSD) of the Elsässer variables $\boldsymbol{z}^{\pm}$ in the sub- and nearby super-Alfvénic regions. The PSD is calculated through the Fourier transform of the correlation function $\mathcal{F}[R(\tau)]$. Power-law fits are performed for both the z^+ and z^- modes when the spectra show a power-law shape on the MHD scale. In all three regions, the spectral index of the z^+ mode is about $-3/2$, and the PSD of the z^- mode is slightly flatter than that of the z^+ mode.

Figure 2 suggests that the turbulent correlation time is significantly different between super- and sub-Alfvénic intervals, especially for the z^- mode. In the sub-Alfvénic interval, the correlation time for the backward z^- mode is the largest (~20 minutes), and it is about 10 times larger than the forward z^+ mode. The correlation time for magnetic fluctuations is the shortest, which is about 102 s in the sub-Alfvén region. In the two super-Alfvénic regions, the correlation time for the forward and backward fluctuations are very close. We also note that the correlation function for the backward z^- mode in all three regions drops dramatically from its maximum value to its value at the first nonzero time lag, which has also been observed at 0.3 au by Helios (Shiota et al. 2017) and 1 au by Wind (Wang et al. 2018). There are two possible reasons for the drop in the z^- correlation time. First, the drop may be caused by noise as the z^- fluctuating power is much lower than the z^+ fluctuating power. This can be seen in the PSD plots as the z^- spectrum flattens significantly at high frequencies ($\geqslant 10^{-2}$ Hz), corresponding to a fast drop in the correlation function at small correlation times. Second, the drop may be physical (Zank et al. 2020, 2022). Due to the observed highly field-aligned flows, the correlation scales in Figure 2 are scales in the direction approximately parallel to the mean field (Bandyopadhyay & McComas 2021; Zhao et al. 2022). As the z^+ and z^- components are governed by different spectral timescales in imbalanced turbulence, it is not surprising that their correlation times/lengths are different. For example, based on the nearly incompressible turbulence model (Zank et al. 2020), the z^+ component may be governed by the nonlinear timescale and the z^- component may be governed by a mix of the nonlinear and Alfvén timescales. The various correlation times are listed in Table 1 as τ_c. It can be seen that the z^+ correlation time is close to the magnetic fluctuation correlation time and is somewhat smaller than the velocity fluctuation correlation time. The z^-

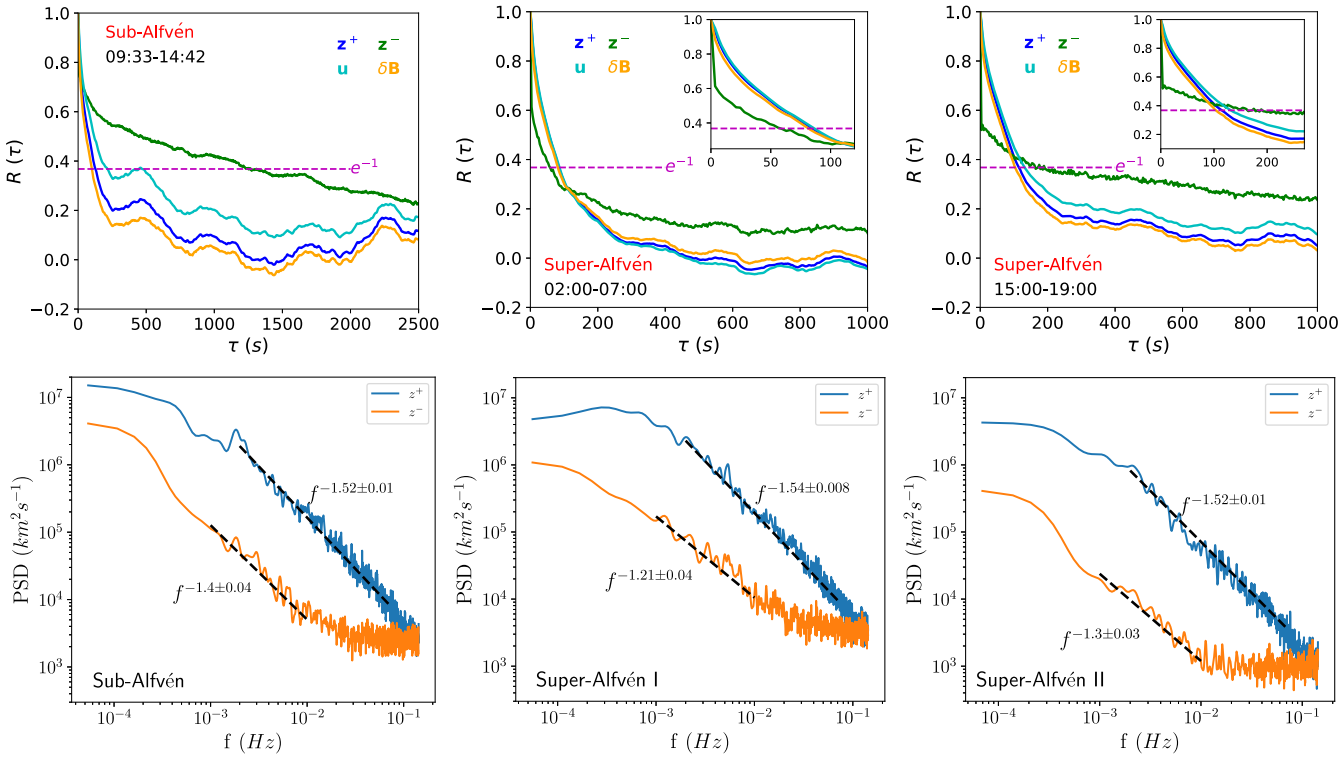

Figure 2. The top three panels show the normalized autocorrelation function for various quantities (z^+, z^-, $\boldsymbol{u}$, and $\delta\boldsymbol{B}$). The horizontal dashed line represents $R(\tau) = 1/e$ at which the correlation time τ_c is determined. The panels from left to right represent the three regions shown in Figure 1. The bottom three panels show the power spectral density of the Elsässer variables $z^{\pm}$ calculated in the sub-Alfvénic and the two nearby super-Alfvénic regions. The black dashed curves represent power-law fitting of the spectra.

Table 1
Correlation Time and Length for Various Fluctuations in the Sub- and Super-Alfvénic Intervals

Interval	Time (UT)	τ_c(s) z^+	τ_c(s) z^-	τ_c(s) $\boldsymbol{u}$	τ_c(s) $\delta\boldsymbol{B}$	L_c(km) z^+	L_c(km) z^-	U_{sc} (km s^{-1})	U_0 (km s^{-1})	V_{A0} (km s^{-1})	Ψ (°)
Sub	09:33-14:42	127	1252	216	102	9.6×10^4	2.6×10^4	400	320	366	15
Super I	02:00-07:00	84	58	86	82	5.6×10^4	8.8×10^3	430	345	257	18
Super II	15:00-19:00	115	163	132	104	5.5×10^4	1.7×10^4	308	238	188	18

Note. τ_c is the correlation time, L_c is the correlation length, $U_{sc} = |\boldsymbol{U}_{sc}|$ is the mean solar wind speed in the spacecraft frame, $U_0 = |\boldsymbol{U}_0|$ is the velocity in the inertial RTN frame, $V_{A0} = |\boldsymbol{B}_0|/\sqrt{4\pi\rho_0}$ is the mean Alfvén speed, and Ψ is the angle between the mean magnetic field $\boldsymbol{B}_0$ and mean velocity field in the spacecraft frame $\boldsymbol{U}_{sc}$. The calculation of L_c takes into account the wave propagation speed.

correlation time is typically larger than the z^+ correlation time, except for the prior super-Alfvénic interval.

We calculate the correlation length for the Elsässer variables $z^{\pm}$ using the modified Taylor's hypothesis (Zank et al. 2022). As the forward Elsässer mode z^+ propagates outward from the Sun ($B_R < 0$), the z^+ mode should have a speed of $U_{sc}\cos\Psi + V_{A0}$ when calculating the associated correlation length, where Ψ is the angle between the mean magnetic field $\boldsymbol{B}_0$ and mean velocity field $\boldsymbol{U}_{sc}$ in the spacecraft frame ($0° \leqslant \Psi \leqslant 90°$), $U_{sc} = |\boldsymbol{U}_{sc}|$, and $V_{A0} = |\boldsymbol{B}_0|/\sqrt{4\pi\rho_0}$ is the mean Alfvén speed. Here, $\boldsymbol{U}_{sc} - \boldsymbol{V}_{psp} = \boldsymbol{U}$ with $\boldsymbol{V}_{psp}$ being the spacecraft velocity. Similarly, the backward propagating z^- mode should use a speed of $|U_{sc}\cos\Psi - V_{A0}|$. These apply for both sub- and nearby super-Alfvénic regions (Zank et al. 2017, 2020, 2022). The results as listed in Table 1 suggest that the z^- correlation length is actually about a quarter of the z^+ correlation length in the sub-Alfvénic interval, despite having a correlation time almost 10 times longer. During the nearby super-Alfvénic intervals, the correlation length for z^- mode is also smaller than the z^+ mode after considering the wave propagation velocity.

4. Cascade Rate

To estimate the turbulence cascade rate, we first consider the Yaglom-like flux calculated by the third-order structure function. The incompressible flux $F_{\rm In}$ is calculated by the third-order mixed structure functions of the Elsässer variables $z^{\pm}$. The energy fluxes for the forward z^+ and backward z^- propagating modes are calculated by

$$Y^{\pm}(\tau) = \langle |\Delta z^{\pm}|^2 \Delta z^{\mp} \rangle, \quad (1)$$

which depends on the time lag τ, and the increments $\Delta z^{\pm}$ of the Elsässer variables are calculated from $\Delta z^{\pm} = z^{\pm}(t+\tau) - z^{\pm}(t)$. The angled bracket $\langle \ldots \rangle$ represents the averaging over time t. The total incompressible energy flux is defined by $F_{In} = (Y^+ + Y^-)/2$. We also calculate the compressible energy

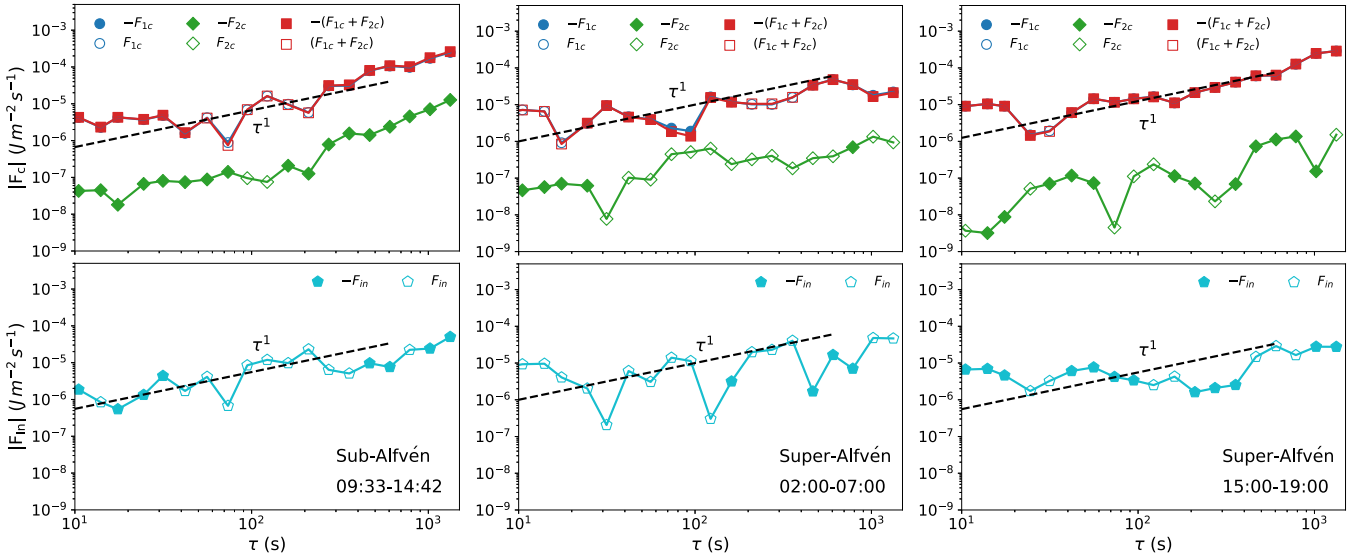

Figure 3. The two terms in the compressible energy flux $|F_{1c}|$ (blue) and $|F_{2c}|$ (green) and their sum $|F_{1c}+F_{2c}|$ (red). The incompressible flux $|F_{In}|$ is plotted as the cyan scatters. All quantities are plotted as a function of the time lag τ. Solid scatters represent negative energy fluxes associated with the forward energy transfer, and hollow scatters denote positive fluxes with inverse energy transfer. The panels from left to right are for sub-Alfvénic, prior super-Alfvénic, and latter super-Alfvénic regions, respectively. The black dashed line in each panel is a reference curve $\propto \tau^1$.

flux using the method suggested by Andrés et al. (2021),

$$F_{1c} = \langle [\Delta(\rho \boldsymbol{U}) \cdot \Delta \boldsymbol{U} + \Delta(\rho \boldsymbol{V_A})] \Delta \boldsymbol{U} - [\Delta(\rho \boldsymbol{U}) \cdot \Delta \boldsymbol{V_A} + \Delta \boldsymbol{U} \cdot \Delta(\rho \boldsymbol{V_A})] \Delta \boldsymbol{V_A} \rangle, \quad (2)$$

$$F_{2c} = 2 < \Delta\rho \Delta e \Delta \boldsymbol{U} > , \quad (3)$$

where $\boldsymbol{V_A} = \boldsymbol{B}/\sqrt{4\pi\rho}$, $e = c_s^2 \log(\rho/\rho_r)$ is the internal energy, $c_s = p/\rho$ is the sound speed, p is the thermal pressure, ρ is the proton mass density, ρ_r is an arbitrary constant reference density, and Δ are the differences at certain time lag τ, such as $\Delta \boldsymbol{U} = \boldsymbol{U}(t+\tau) - \boldsymbol{U}(t)$. An isothermal closure is assumed in deriving the above formula for the compressible energy flux. The total compressible energy flux is the sum of the two terms, i.e., $F_{1c} + F_{2c}$. In the incompressible limit, the first term F_{1c} reduces to the incompressible flux $F_{\rm In}$ and the second term F_{2c} vanishes.

In Figure 3, the two compressible fluxes F_{1c} and F_{2c} are plotted in the top panels as the blue and green scattered lines, and their sum as the red scattered lines. Note that the red line overlaps with the blue line, indicating the dominance of the F_{1c} in the total compressible flux. The total incompressible flux $F_{\rm In}$ is plotted as the cyan scattered line in the bottom panels. The left panel is for the sub-Alfvénic interval. The middle and right panels are for the two nearby super-Alfvénic intervals. The black dashed lines in each panel display a reference linear relation between the energy fluxes and time lag, which is expected for inertial range turbulence with a scale-independent energy transfer rate. We plot the absolute values of the fluxes in logarithmic scale following previous studies (e.g., Bandyopadhyay et al. 2020; Andrés et al. 2021; Sorriso-Valvo et al. 2021). The positive and negative energy fluxes are distinguished by solid and hollow markers. We note that, in principle, the sign of the energy flux indicates the direction of energy flow through the scales: negative fluxes correspond to the forward cascade where the energy is transferred from large to small scales, and a positive sign in the energy flux means an inverse cascade (energy transferred from small to large scales). However, as noted elsewhere (e.g., Sorriso-Valvo et al. 2021), the third-order structure function may oscillate between positive and negative values in solar wind data, thus indicating no convergence either because of low statistics or not yet developed turbulence. As shown in the figure, the incompressible energy fluxes $F_{\rm In}$ tend to show more oscillations between positive and negative values. However, in spite of few sign changes, a negative compressible energy flux is prevalent in the sub-Alfvénic region (and in the downstream super-Alfvénic interval), thus pointing to a large-to-small scale energy transfer. In addition, the compressible energy fluxes in three regions are more consistent with τ^1 linear scaling at the time lags within the inertial range. This may suggest that compressible effects are not negligible for the energy transfer in these intervals. In all cases, the second compressible term F_{2c} is negligible compared to the first term F_{1c}.

Figure 3 plots the fluxes as functions of the time lag. Converting time lags τ to length increments l requires Taylor's hypothesis, where the two quantities are related by the solar wind speed in the spacecraft frame $l = U_{\rm sc}\tau$. As the Alfvén speed is no longer negligible in the three intervals selected here, we need to consider the modified Taylor's hypothesis. This is important for more accurately estimating the energy cascade rates. As described in Section 3, the forward flux Y^+ should have a speed of $U_{\rm sc}\cos\Psi + V_{A0}$ when calculating the associated length increments, and the backward flux Y^- should have a speed of $|U_{\rm sc}\cos\Psi - V_{A0}|$.

In Figure 4, the top three panels show the forward and backward incompressible fluxes $Y^{\pm}$ as functions of the length increments l, which are normalized by the ion inertial length $d_i = c/\omega_{\rm pi}$, where c is the speed of light and $\omega_{\rm pi}$ is the ion plasma frequency. Similar to Figure 3, positive and negative fluxes are distinguished by solid and hollow symbols. The incompressible energy fluxes Y^+ in the sub-Alfvénic and two super-Alfvénic regions are roughly consistent with a l^1 slope. For the energy fluxes Y^-, there is only a limited range of scales for which the calculation is reliable as, at small scales ($\tau \leqslant 100\,s$), z^- is possibly overpowered by noise, as shown in

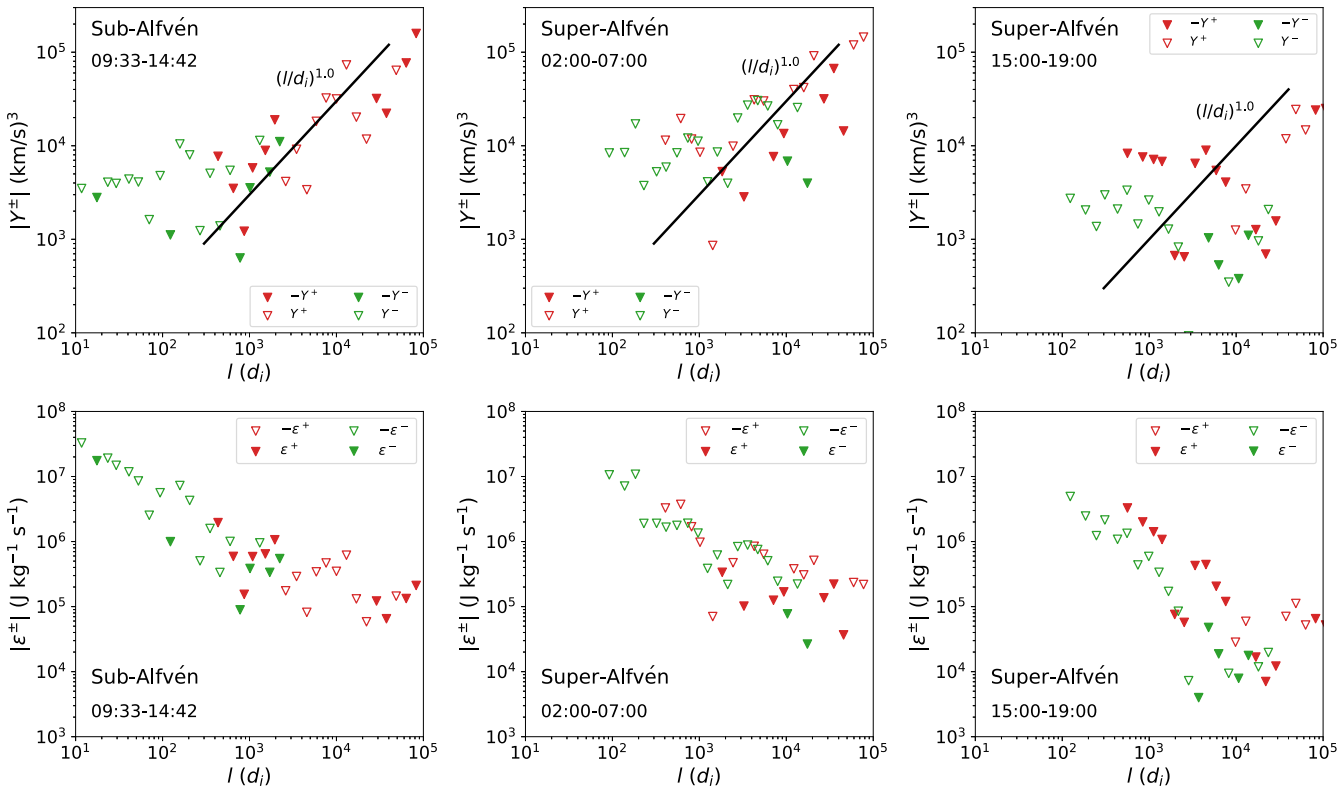

Figure 4. The top three panels show the incompressible energy flux for the forward and backward Elsässer modes, $Y^{\pm}$. A modified Taylor's hypothesis is used to convert the time lag to the length scale l, normalized to the ion inertial length d_i. A linear relation between the fluxes and the length increment $l^{1.0}$ is displayed for reference. The bottom three panels show the energy cascade rate $\epsilon^{\pm}$ associated with the forward and backward fluxes $Y^{\pm}$, plotted as functions of the length scale l. Solid symbols represent a negative energy flux and forward energy cascade, and hollow symbols denote a positive energy flux and inverse energy cascade.

Figure 2. We note that the flux amplitude is smaller in the downstream super-Alfvénic interval compared to the other two intervals. This is because this interval has a higher density and smaller velocity and magnetic field fluctuations, which also leads to a weaker energy cascade rate per unit mass.

The Politano–Poquet law suggests that the combination of Elsässer fluxes $Y^{\pm}$ at the length increment of l are proportional to the energy cascade rate as

$$(Y^+ + Y^-)/2 = -\frac{3}{4}\varepsilon l. \quad (4)$$

Based on this relation, the energy cascade rate ε can be calculated. The bottom three panels in Figure 4 show the incompressible energy cascade rates as functions of the length increment l. Equation (4) can be extended for the isothermal compressible case as well after replacing $(Y^+ + Y^-)/2$ by $(F_{1c} + F_{2c})/\rho_0$, where ρ_0 is the average mass density (Andrés et al. 2021). Because of the modified Taylor's hypothesis, the forward and backward energy cascade rates at the same time lag correspond to different length increments.

To calculate the average energy cascade rate, we perform a linear fit with zero intercept to the total compressible fluxes as they exhibit better linear scaling and generally negative values compared to the incompressible energy flux, as shown in Figure 3. The fitting timescale ranges from ~100 to 600 s. We also calculate the coefficient of determination R^2 for the fits (Coburn et al. 2014, 2015). The R^2 value indicates the goodness of fit, as $R^2 \sim 1$ corresponds to a good fit. The numbers are listed below. The averaged compressible cascade rate per unit mass for the sub-Alfvénic region is about 5.7×10^5 J kg^{-1}s^{-1} ($R^2 = 0.70$), for the prior super-Alfvénic region about 1.5×10^5 J kg^{-1}s^{-1} ($R^2 = 0.27$), and for the latter super-Alfvénic region also about 1.5×10^5 J kg^{-1}s^{-1} ($R^2 = 0.94$). As mentioned earlier, the higher plasma density and smaller velocity and magnetic field fluctuations shown in Figure 1 may explain the low value of the cascade rate in the latter super-Alfvénic interval. On the other hand, in the prior super-Alfvénic interval, the fluctuation amplitude is comparable to that of the sub-Alfvénic region, but the averaged cascade rate is about a quarter of that of the sub-Alfvénic region. However, as the value of R^2 in this interval is too small, which may be caused by oscillations between positive and negative energy fluxes possibly due to undersampling, we cannot draw important conclusions about the averaged cascade rate from this prior super-Alfvénic interval.

5. Conclusions

In this letter, we present an analysis of the turbulence cascade rate and correlation function in the sub-Alfvénic solar wind observed by the Parker Solar Probe during Encounter 8. The results are compared with two super-Alfvénic intervals nearby. The main conclusions are listed as follows.

1. A modified Taylor's hypothesis that accounts for wave propagation is adopted to convert time lags to length increments in calculating the correlation length of Elsässer variables. This is especially important when the Alfvén speed is comparable to the solar wind proton speed.

2. The correlation time and correlation length for Elsässer variables is larger in the sub-Alfvénic interval, especially for the inward propagating z^- mode.
3. The correlation length of the z^- mode is shorter than that of the outward propagating z^+ mode in the sub-Alfvénic region, although the correlation time of z^- mode is much longer. In two nearby super-Alfvénic intervals, the correlation length of the z^- mode is also smaller than that of the z^+ mode when considering the wave propagation speed.
4. We calculate the scale-dependent energy flux using both compressible and incompressible formalisms. Using the modified Taylor's hypothesis, we calculate the energy cascade rate per unit mass for the forward and backward incompressible modes. The averaged energy cascade rate based on the total compressible energy flux is larger in the sub-Alfvénic interval than the two nearby super-Alfvénic regions. However, the coefficient of determination R^2 calculated in the prior super-Alfvénic interval is less than 0.5, and we caution not to draw important conclusions from this particular interval.

There are a few caveats to the current analysis that we would like to discuss. First, the latter super-Alfvénic interval studied in this letter has a smaller solar wind velocity and slightly shorter interval length compared to the other two regions, which may cause some differences in the results. Second, the averaged energy cascade rates are calculated using the standard Taylor's hypothesis without considering wave propagation effects, so the number may not be accurate. Third, the longest sub-Alfvénic interval observed to date (Kasper et al. 2021) is about 310 minutes. With approximately 5300 data points in each interval, the maximum order of the meaningful structure function is approximately 3 (Dudok de Wit 2004). Therefore, the statistics for the third-order structure function used in this work is marginally sufficient. However, we caution the reader that the oscillation in energy fluxes may still be due to undersampling. Fourth, the cascade rate in a single event is not sufficient to compare the sub-Alfvénic and super-Alfvénic regions in general; in addition, the energy transfer mechanism is more complex (Coburn et al. 2014, 2015) than the simple formulations we consider here. Finally, the use of Yaglom-like laws requires the turbulence to be isotropic, which is likely not satisfied in reality. This is also a caveat of the present study. However, our results are still novel and important, being the first such measurements in the sub-Alfvénic solar wind. The current data are not sufficient for a statistical significance test, which is left for future investigations after more data on the sub-Alfvénic wind have been accumulated.

The energy cascade rates associated with forward and backward modes can be calculated using a modified Taylor's hypothesis. However, the constant energy cascade rate assumption is not well satisfied for the forward and backward Elsässer modes. Finally, we emphasize that the use of a modified Taylor's hypothesis has significant effects on the results. The much longer correlation time of the z^- mode actually corresponds to a shorter or comparable correlation length than the z^+ mode. This is important for future investigations of PSP data near the Sun.

We acknowledge the partial support of the NSF EPSCoR RII-Track-1 Cooperative Agreement OIA-1655280, a NASA award 80NSSC20K1783 and a NASA Parker Solar Probe contract SV4-84017. D.T. was partially supported by the Italian Space Agency (ASI) under contract 2018-30-HH.0. The Parker Solar Probe was designed, built, and is now operated by the Johns Hopkins Applied Physics Laboratory as part of NASA's Living with a Star (LWS) program (contract NNN06AA01C). Support from the LWS management and technical team has played a critical role in the success of the Parker Solar Probe mission.

ORCID iDs

L.-L. Zhao https://orcid.org/0000-0002-4299-0490
G. P. Zank https://orcid.org/0000-0002-4642-6192
D. Telloni https://orcid.org/0000-0002-6710-8142
M. Stevens https://orcid.org/0000-0002-7728-0085
J. C. Kasper https://orcid.org/0000-0002-7077-930X
S. D. Bale https://orcid.org/0000-0002-1989-3596

References

Adhikari, L., Zank, G. P., & Zhao, L. 2021, Fluids, 6, 368
Adhikari, L., Zank, G. P., & Zhao, L.-L. 2020, ApJ, 901, 102
Andrés, N., Sahraoui, F., Galtier, S., et al. 2019, PhRvL, 123, 245101
Andrés, N., Sahraoui, F., Hadid, L. Z., et al. 2021, ApJ, 919, 19
Bale, S. D., Goetz, K., Harvey, P. R., et al. 2016, SSRv, 204, 49
Bandyopadhyay, R., Goldstein, M. L., Maruca, B. A., et al. 2020, ApJS, 246, 48
Bandyopadhyay, R., Matthaeus, W. H., McComas, D. J., et al. 2022, ApJL, 926, L1
Bandyopadhyay, R., & McComas, D. J. 2021, ApJ, 923, 193
Banerjee, S., & Kritsuk, A. G. 2018, PhRvE, 97, 023107
Bourouaine, S., & Perez, J. C. 2018, ApJL, 858, L20
Bruno, R., & Carbone, V. 2013, LRSP, 10, 2
Chen, C. H. K., Bale, S. D., Bonnell, J. W., et al. 2020, ApJS, 246, 53
Coburn, J. T., Forman, M. A., Smith, C. W., Vasquez, B. J., & Stawarz, J. E. 2015, RSPTA, 373, 20140150
Coburn, J. T., Smith, C. W., Vasquez, B. J., Forman, M. A., & Stawarz, J. E. 2014, ApJ, 786, 52
Dudok de Wit, T. 2004, PhRvE, 70, 055302
Elsasser, W. M. 1950, PhRv, 79, 183
Frisch, U. 1995, Turbulence. The legacy of A.N. Kolmogorov (Cambridge: Cambridge Univ. Press) https://ui.adsabs.harvard.edu/abs/1995turb.book.....F/abstract
Goldstein, M. L., Roberts, D. A., & Matthaeus, W. H. 1986, JGR, 91, 13357
Kasper, J. C., Abiad, R., Austin, G., et al. 2016, SSRv, 204, 131
Kasper, J. C., Klein, K. G., Lichko, E., et al. 2021, PhRvL, 127, 255101
Klein, K. G., Perez, J. C., Verscharen, D., Mallet, A., & Chandran, B. D. G. 2015, ApJL, 801, L18
Kolmogorov, A. 1941, DoSSR, 30, 301 https://ui.adsabs.harvard.edu/abs/1941DoSSR..30..301K/abstract
Moncuquet, M., Meyer-Vernet, N., Issautier, K., et al. 2020, ApJS, 246, 44
Perez, J. C., Bourouaine, S., Chen, C. H. K., & Raouafi, N. E. 2021, A&A, 650, A22
Politano, H., & Pouquet, A. 1998, GeoRL, 25, 273
Shiota, D., Zank, G. P., Adhikari, L., et al. 2017, ApJ, 837, 75
Sorriso-Valvo, L., Carbone, F., Perri, S., et al. 2018, SoPh, 293, 10
Sorriso-Valvo, L., Yordanova, E., Dimmock, A. P., & Telloni, D. 2021, ApJL, 919, L30
Wang, X., Tu, C. Y., He, J. S., et al. 2018, JGRA, 123, 57
Zank, G., Adhikari, L., Hunana, P., et al. 2017, ApJ, 835, 147
Zank, G., Nakanotani, M., Zhao, L.-L., Adhikari, L., & Telloni, D. 2020, ApJ, 900, 115
Zank, G. P., Dosch, A., Hunana, P., et al. 2012, ApJ, 745, 35
Zank, G. P., Zhao, L. L., Adhikari, L., et al. 2022, ApJL, 926, L16
Zhao, L.-L., Zank, G., Hu, Q., et al. 2021, A&A, 650, A12
Zhao, L. L., Zank, G. P., Adhikari, L., et al. 2020, ApJS, 246, 26
Zhao, L. L., Zank, G. P., Adhikari, L., & Nakanotani, M. 2022, ApJL, 924, L5
Zhao, L. L., Zank, G. P., He, J. S., et al. 2021, ApJ, 922, 188